

THE MULTI-COLORED HOT INTERSTELLAR MEDIUM OF “THE ANTENNAE” GALAXIES (NGC 4038/39)

G. FABBIANO, M. KRAUSS, A. ZEZAS, A. ROTS

Harvard-Smithsonian Center for Astrophysics,
60 Garden Street, Cambridge, MA 02138

AND S. NEFF

Laboratory for Astronomy and Solar Physics,
NASA / Goddard Space Flight Center, Greenbelt, MD 20771

Draft version November 1, 2018

ABSTRACT

We report the results of the analysis of the extended soft emission discovered in the *Chandra* ACIS pointing at the merging system NGC4038/39 (the Antennae). We present a ‘multi-color’ X-ray image that suggests both extensive absorption by the dust in this system, peaking in the contact region, as well as variations in the temperature of different emitting regions of the hot interstellar medium (ISM). Spectral fits to multi-component thermal emission models confirm this picture and give a first evaluation of the parameters of the hot plasma. We compare the diffuse X-ray emission with radio continuum (6cm), HI, CO, and H α images to take a first look at the multi-phase ISM of the Antennae galaxies. We find that the hot (X-ray) and cold (CO) gas have comparable thermal pressures in the two nuclear regions. We also conclude that the displacement between the peak of the diffuse X-ray emission in the north of the galaxy system, towards the inner regions of the northern spiral arm (as defined by H α , radio continuum and HI), could result from ram pressure of infalling HI clouds.

Subject headings: galaxies: peculiar — galaxies: individual (NGC 4038/39, Antennae) — galaxies: interactions — X-rays: galaxies

1. INTRODUCTION

This is the fifth in a series of papers based on the first *Chandra* ACIS-S (Garmire 1997; Weisskopf et al 2000) observation of the Antennae galaxies (NGC4038/39). The first paper in this series gives a general picture of the overall results of this 72.2 ks. observation (ObsID 315: Fabbiano et al 2001 – Paper I). The following three papers (Zezas et al 2002a, b – Paper II, III; Zezas & Fabbiano 2002 – Paper IV) discuss the properties of the point-like source population detected in this merging system. Here, we concentrate on the analysis of the complex diffuse soft emission reported in Paper I and on its importance for our understanding of the hot ISM of these galaxies.

The Antennae (dynamically modeled by Toomre & Toomre 1972 and Barnes 1988) are the nearest pair of colliding galaxies involved in a major merger (D = 19 Mpc for H₀ = 75 km s⁻¹ Mpc⁻¹¹). Hence, this system provides a unique opportunity for getting the most detailed look possible at the consequences of a galaxy merger as evidenced by induced star formation and the conditions in the ISM. Each of the two colliding disks shows rings of giant H II regions and bright stellar knots with luminosities up to M_V ∼ -16 (Rubin et al 1970), which are resolved with the *Hubble Space Telescope* into typically about a dozen young star clusters (Whitmore & Schweizer 1995, Whitmore et al 1999). These knots coincide with the peaks of H α , 2.2 μ , and 6-cm radio-continuum emission (Amram et al 1992; Stanford et al 1990; Neff & Ulvestad 2000), indicating an intensity of star formation in each single region exceeding that observed in 30 Doradus. CO aperture syn-

thesis maps reveal major concentrations of molecular gas, including $\sim 2.7 \times 10^9 M_{\odot}$ in the region where the two disks overlap (Stanford et al 1990; Wilson et al 2000). A recent K-band study derives ages for the star clusters ranging from 4 to 13 Myr, and measures high values of extinction ($A_V \sim 0.7 - 4.3$ mag; Mengel et al 2000).

The presence of an abundant hot ISM in the Antennae was originally suggested by the first *Einstein* observations of this system (Fabbiano & Trinchieri 1983), and has been revisited with all following major X-ray telescopes (ROSAT: Read et al 1995, Fabbiano et al 1997; and ASCA: Sansom et al 1996). The ROSAT HRI image was used in a recent multiwavelength study of the Antennae by Zhang et al (2001), which suggests feedback between star clusters and the interstellar medium (ISM). The *Chandra* observation gives us the means to study this hot ISM in unprecedented detail. The spatial resolution of *Chandra* is at least 10 times superior to that of any other X-ray observatory, allowing us to resolve the emission on physical sizes of ∼ 47 pc for D=19 Mpc. With this resolution we have detected individual X-ray sources down to $L_X \sim 10^{38}$ ergs s⁻¹ (Paper II) and we can image in detail the spatial properties of more extended emission regions (see Paper I). At the same time, ACIS allows us to study for the first time the X-ray spectral properties of these emission regions, providing additional important constraints on their nature.

Our initial look at these *Chandra* data (Paper I) revealed a complex, diffuse and soft emission component responsible for about half of the detected X-ray photons from the

¹ We have adopted this distance for conformity with most recent work on the Antennae; in Papers I-III, a distance of 29 Mpc, H₀ = 50 km s⁻¹ Mpc⁻¹ was used; in Paper IV we discuss our results using both D = 19 and 29 Mpc

two merging galaxies. The X-ray spectrum of this component exhibits emission lines, pointing to optically thin gaseous emission. In the present paper, we explore further the spectral/spatial properties of this emission and its relation to the multi-phase ISM: in §2 we present a ‘true-color’ X-ray image of the extended emission (i.e., an image where the color scale represents the photon energy), in §3 we present a spectral fitting analysis of these data, and in §4 we describe new 4 and 6cm radio images derived from archival radio data, matched to the effective resolution of the diffuse X-ray emission. In §5 we discuss the physical properties of the hot ISM and we compare the diffuse X-ray emission with H α , radio continuum (6cm), HI and CO data.

2. THE TRUE-COLOR X-RAY IMAGE

Chandra was pointed to NGC4038/39 on December 1, 1999, for 72.2 ks with the back-illuminated ACIS-S3 CCD chip at the focus. The observations and data reduction and screening are described in Paper I. We used CIAO 2.2.1 and other software developed for the purpose in the present data analysis.

We have used these data to produce a true-color X-ray image of the Antennae that would be sensitive to spectral differences in the soft diffuse emission. The true-color X-ray image of Paper I showed that the diffuse emission is soft (mostly at energies below 2 keV) and thus differentiated it from the harder broad-band emission of the point-like sources, but did not have the resolution to show spectral differences in this soft emission. To obtain this resolution, we cut the data into energy bands of 0.3-0.65, 0.65-1.5, and 1.5-6 keV. These bands were chosen using thermal plasma models as a reference: the low energy band does not include the Fe-L blend seen around 1 keV, whereas the high energy band should include only the hottest (or most highly absorbed) material. The resulting images were then adaptively smoothed using the tool *csmooth* with a minimal significance (S/N) of 3.5 and maximum significance (S/N) of 5.0. This tool uses different smoothing scales to enhance low-surface-brightness extended features, while retaining the resolution allowed by the areas of the image with the highest signal-to-noise ratios.

Monochromatic exposure maps were created for each of the bands at 0.5, 1, and 3 keV, and smoothed using the same smoothing scales as the images. The images were then divided by the corresponding exposure map and combined using *dmimg2jpg* to create a “true-color” image, with a red to blue progression to represent increasing photon energy (Fig. 1).

To derive a true-color image of the diffuse emission, we then proceeded to identify and remove point-like sources. A source list was first generated using the *wavdetect* tool, using scales of 1, 1.4, 2, 2.8 and 4 pixels; the initial list was then culled to include only obvious point sources. These are sources 1, 2, 3, 4, 11, 12, 13, 14, 16, 18, 19, 20, 21, 23, 29, 31, 32, 33, 34, 35, 37, 38, 41, 42, 43, 44, 46, 47, 49, from the list of Paper II. Background regions were created to best represent the local diffuse emission. The tool *dmfilth* (*dmFillTheHole*) was run in each of the three spectral band images to fill in the source regions with pixel values sampled from the Poisson distribution whose mean was that of pixel values in the corresponding background re-

gion. The same procedure described above of smoothing, exposure correction and combining of the three resulting images into a true-color image was then followed. The result is shown in fig. 2.

While figs. 1, 2 do not give a quantitative assessment of the spectral properties, because the color scale is not linear and has been enhanced to show faint features, it is clear from them that there are spectral variations throughout. In particular, the area of impact between the two galaxies [centered approximately on RA(J2000)=12 h 01 m 55 s and Dec(J2000)=−18 $^{\circ}$ 52 $'$ 50 $''$] releases only high energy photons, as it would be expected in the presence of large amounts of obscuring material. The nuclear regions, as already suggested in Paper I, include harder emission (‘white’ in figs 1, 2) than other relatively unobscured regions of the ISM.

3. SPECTRAL ANALYSIS OF THE DIFFUSE X-RAY EMISSION

To derive quantitative information on the spectral differences suggested by the color maps, we performed a spectral analysis of the diffuse emission. We screened the data for all the point-like sources reported in Paper II. We retained the sources with a strong extended component. These are sources 5, 6, 7, 10, 25 of Paper II. Fig. 3a shows a raw image of the Antennae together with the excised source regions. We did not correct for the amount of diffuse emission which was also excised together with the excluded sources. This does not affect the parameters of the fit (temperature, N_H, photon index, abundance) but results in lower normalizations (or emission measure in the case of a thermal model).

To derive quantitative information on the varying spectral properties suggested by the color image, we first divided the area in a grid, so to perform a systematic spectral analysis from which we could derive a first-cut spectral map of the hot ISM. In order to have at least 100 in each extracted spectrum (before background removal), we used regions 50 × 50 pixels (24.5 $''$ × 24.5 $''$) in size. Using fig. 2 as a guide, we then focused on the regions with the largest number of counts (highest signal to noise) to perform a more in depth analysis. Both grid and individual regions (ellipses) are shown superimposed on the color map of the diffuse emission in fig. 3b.

For each region (either square in the grid, or ellipse) we extracted photon invariant (PI) spectra and created weighted response matrices (RMFs) and ancillary response files (ARFs) using the *acisspec* script of CIAO v2.1. This script invokes the *dmextract* tool to extract the spectrum and then the *mkwrmf* and *mkwarf* tools in order to create area weighted RMF and ARF files for each region, since they span more than one Fits Embedded Function (FEF) regions. The spectra were then grouped to have at least 15 counts per bin in order to use χ^2 statistic for the fits. From the spectrum of the diffuse emission presented in Paper I, is clear that most photons are below 5 keV. Therefore in order to minimize contamination by the background which dominates above 7 keV we ignored any data outside the 0.3-7.0 keV energy range. For the spectral fits we used the XSPEC v10.0 spectral fitting package (Arnaud et al. 1996). All the cited errors for the spectral parameters are for the 90% confidence level for one interesting

parameter, unless otherwise stated. The background was obtained from source free regions outside the galaxy.

3.1. Spectral ‘Map’

First we attempted fits with an absorbed single thermal plasma model (RS model; Raymond & Smith 1977) and solar abundances (the abundance table by Anders & Grevesse 1989 was used). For these fits the absorbing column density was free to vary above the Galactic $N_H = 3.4 \times 10^{20} \text{ cm}^{-2}$ (Stark et al. , 1992). Typical best-fit kT is between 0.1 keV and 0.9 keV and best-fit N_H can reach as high as $\sim 8 \times 10^{21} \text{ cm}^{-2}$. However, these fits were unacceptable in all but 6 cases (reduced χ^2 greater than 1.4). Letting the metal abundance vary as a free parameter in the fits (with the relative abundances fixed at the solar ratio) increased the number of fits with acceptable χ^2 , but the fit is still unacceptable for the majority of the spectra. The values of the abundances suggested by the fits were uniformly subsolar (~ 0.1).

Since a single thermal component model is clearly not an adequate representation of the data, we introduced a second thermal component with a different absorbing column density [RS-(RS) model; here and in the following models the parentheses indicate the absorbed component]. We first again assumed solar abundances, and we then let the abundance vary in both components. In both cases, the overall N_H was free to vary above the Galactic value.

The two-component, solar abundance, model provided a statistically significant improvement in the fit (above the 99.9% confidence level based on an F-test for two additional parameters; Bevington & Robinson, 1992) in all but 6 cases, over the single component, solar abundance model. In most cases the overall absorbing column is very close to the Galactic N_H and the low temperature component has a typical kT of 0.2-0.3 keV. The second component is typically seen through a larger column density ($N_H \sim 2 - 8 \times 10^{21} \text{ cm}^{-2}$), and has a higher temperature than the unabsorbed component ($kT \sim 0.7 - 0.8 \text{ keV}$). The results from these fits are presented in Table 1: Column (1) gives the data extraction region following the notation of fig. 3b, Column (2) gives the net number of counts in each region (together with the statistical error), Column (3) gives the overall N_H in units of 10^{22} cm^{-2} , Column (4) gives the temperature for the first component, while Columns (5) and (6) give the column density and the temperature for the second (absorbed) component. Column (7) gives the ratio of the emission measures of the two best-fit thermal components. Column (8) gives the χ^2 and the number of degrees of freedom (dof). For the regions where a single component model gives an acceptable fit only the parameters for this model are listed. Fig. 4 presents the 99% confidence contours for the two interesting parameters N_H and kT . Red and blue contours identify the low and high temperature components respectively. The crosses mark the best fit values for each component; if the crosses are not shown the best fit values fall outside the range of the plot. Here, as in all the spectral fit tables, the confidence regions are calculated using the $\Delta\chi^2$ method, therefore they are a strong constraint only in the case of acceptable fits (i.e. when the model is a reliable representation of the data). Regions 2C, 2E, 3E and 5C have unacceptable χ^2 in the solar abundance

fit. These areas are part of the luminous emission regions addressed in greater detail in §3.2. In two instances in Table 1 (and Table 2) the best-fit kT of the low temperature component is below 0.1 keV (i.e. outside the range of ACIS). However, in these cases the upper bound is typically well within the instrumental range. These results should be considered conservatively as upper limits on the temperature.

The results of the fits with the abundance as a free parameter in each thermal component are listed in Table 2. Although the χ^2 are slightly improved, the fits are still not acceptable in the bins with a larger number of counts. The best-fit temperatures, although not identical, are in the general range of those obtained for the solar abundance fits. The abundance is either ill-defined or subsolar [abundances are listed in Cols. (4) and (7)]. Whenever a minimum is found, we list it with the errors. In some cases, a minimum is found, but the confidence region extends outside one of the fit boundaries (0-5 for Z ; 0-64 keV for kT ; $> 3.4 \times 10^{20} \text{ cm}^{-2}$, the line of sight value, for the total N_H). In these cases, we list both the value of the parameter in question at the minimum χ^2 and the bound that can be determined from the explored grid. If no minimum is found, we give the bound calculated on the basis of the fitting grid boundary where the lowest value of χ^2 is registered. In the case of the abundance, large values typically occur in unconstrained cases, either because a minimum was not found in the χ^2 distribution, or, if a minimum was found, because the error is of the order of magnitude of the best fit value. Some values of N_H returned by the fit (e.g. for regions 5-D and 5-E) are extremely large, but also have comparably larger errors, indicating that they are likely to be a consequence of poor statistics. In the case of region 5-E, the extreme value of N_H is not found when other models are adopted (e.g. see Table 1). Similarly, the ratios of best-fit emission measures (both Table 1 and 2) show a few extreme values. This occurs for regions 2-A, 5-E (both tables), and 2-E, 5-D (Table 2), indicating that one of the two components is likely to be an artifact of the fit.

We also fitted the data with a composite thermal plasma + power-law model (RS+PO). The rationale for this model is that there could be a significant unresolved X-ray binary component to the emission, with fluxes below the detection threshold of our data (see Paper II; the corresponding luminosity is near $10^{38} \text{ ergs s}^{-1}$). This model gave consistently worse χ^2 than the two-thermal-plasma model.

In summary, we conclude that this first fitting exercise strongly suggests a complex temperature distribution in the ISM, at least in all the regions with higher count statistics.

3.2. Four Luminous Emission Regions

Although the spectral grid gives a quantified version of the color image, showing spectral variability throughout the soft emission, and suggesting a multi-temperature ISM, the division of the data in a grid cuts some of the features of the ISM in a way that it is not optimal. We have therefore selected four regions, identified in fig. 3b, for further study. These regions are associated with the two nuclei and the chain of hotspots to the West of the northern nucleus (NGC 4038). In fig. 3b they are marked as N

for the northern nucleus (NGC 4038), S for the southern nucleus (NGC 4039), and R1 and R2 for the two hotspots to the West of the northern nucleus. The emission peak in the S region was excised, because it corresponds to a point-like source (Paper II).

We repeated the fitting procedures used for the binned array, using again on these regions the RS+(RS) and RS+(PO) model, with both solar abundance and with the abundance as a free parameter. In the assumption of solar abundance, neither model gave an acceptable fit to the spectrum of any region but R2, which is also the region with the smallest number of spectral counts (see Table 3). We therefore did not pursue further analysis for R2. The results from these fits are summarized in Tables 3 and 4.

Again, the introduction of the abundance as a free parameter leads to improved, but still not good, fits. Preferred values of the abundance are subsolar. This results is understandable if we look at fig. 5, that shows the best fit RS+(RS) solar abundance model together with the residuals for these four regions. The model soft component tends to have a more pronounced peak in the region below 1 keV than the data. This is the regions of more prominent Fe-L emission. With the exclusion of the RS+[PO] model for the two nuclei, the improvement of the fit over the solar abundance models was statistically significant above the 99% confidence level based on an F-test.

Fits to 3-component models, with fixed solar abundance (Table 5), give improved χ^2 at a level similar to those of the free abundance 2-component fits. These models consist of two thermal RS components and either a power-law (PO) or a third RS component. One of the RS components is either absorbed by the same column as the power-law [RS+(RS+PO) model] or just by the foreground column [RS+RS+(PO) model]. Similarly, in the 3-RS component models, we also explored the possibility that the second thermal component is associated either with the foreground or with the obscured thermal component: these are noted as RS+RS+(RS) and RS+(RS+RS) respectively.

All models gave similar χ^2 , with the exception of the southern nucleus, where the 2-RS+PO models are slightly favored. The best fit temperatures for the two thermal components are $kT \sim 0.2 - 0.3$ keV and $kT \sim 0.7 - 0.9$ keV respectively, and the slope of the power-law is $\Gamma \sim 3$. These power-laws are steeper than expected from unresolved X-ray binaries (where $\Gamma \sim 2$ are more the norm; e.g. Schulz 1999, Yokogawa et al 2000). The results from the three thermal component models are also presented in Table 5. While two of the components are in the range found by the previous fits, the third component tends to be rather hard, and could be suggestive of unresolved hard sources.

The range of models used are still not adequate to fit the spectra with the largest number of counts (southern nucleus and region R1, in that order). We further explored the worst-fit, highest counts southern nucleus, by allowing for the abundance to vary in the RS+(RS+PO) model. However, this did not help the fit ($\chi^2 = 95.8/63$), and it led to totally unconstrained results for the power-law and the abundance of the soft component. We also divided the

southern nucleus region in two sub-regions, one including the E-W bar-like feature (see fig. 2), but we did not get appreciably different results within statistics; the results are consistent with those of Table 5.

These result suggest complex emission regions. The different fits, both with solar abundance and with the abundance as a free parameter, suggest two principal temperatures of the hot ISM: $\sim 0.2 - 0.3$ keV and $\sim 0.6 - 0.8$ keV. The abundance is either ill-defined or subsolar. Subsolar abundances were also reported by Sansom et al (1996) from the spectral analysis of the integrated ASCA spectrum of The Antennae. At this point, we believe that one should be cautious in over-interpreting these possible subsolar abundances, given that the complexity of the emission regions, and the relative low spectral resolution of the CCD data could conspire in giving erroneously lower abundances (see e.g. demonstration in Kim & Fabbiano 2003; Weaver et al 2000; Matsushita et al 1997). Moreover, the elemental abundances were fixed at the solar ratio, and this may not hold in a starburst regions with a prevalently young and evolving massive stellar population, where Iron may be under-abundant, because of the prevalence of SN II. Finally, uncertainties in the line emission models themselves may conspire in giving an erroneously higher continuum, if the data are not of sufficient spectral resolution. Given the obvious spectral complexity of this ISM, and the relatively limited spatial resolution, resulting from the need to integrate the spectra over sizeable areas, we believe that delving deeper in the abundance problem is not warranted by these data.

In Table 6 we give the emission measures for the fits of Table 4 (EM^2) and power-law (PO) normalization for the three component models, together with the absorption-corrected luminosity in the 0.1 - 10.0 keV band for each component.

4. LOW-RESOLUTION 4CM AND 6CM RADIO MAPS

Since we do not see sharp features in the hot ISM, possibly because of the relatively low statistics of the X-ray data, we have re-analyzed radio wavelength observations to produce images of the diffuse radio emission, on scales similar to those of our true-color X-ray map (fig. 2).

VLA³ archival data (20, and 6cm) were used together with 6cm observations from Neff & Ulvestad (2000) to produce images sensitive to a range of spatial scales. The standard source 3C286 was used to set the flux density scale, and the source 1159-2148 was used as a phase calibrator. Each data set was edited, calibrated, imaged, and then self-calibrated using standard image processing techniques and the Astronomical Image Processing System (AIPS). Data sets observed using B1950 coordinates were precessed to the J2000 system. Data sets from different arrays were then combined and self-calibrated. Data weighting was adjusted to produce images of the desired angular resolution. Image deconvolution (CLEANing) included the removal of four background radio sources within the telescope's primary beam response. Because our final images are made from multiple data sets, some with unknown information about weather during the observations, we conservatively

² $EM = \int n^2 dV$ where n is the density, V is the volume of the gas

³ The Very Large Array (VLA) is operated by the National Radio Astronomy Observatory (NRAO), which is a facility of the National Science Foundation operated under cooperative agreement by Associated Universities, Inc.

assume a flux calibration error of 5%. Absolute position errors of the brighter radio sources are less than $0.15''$. 20 and 6cm images are shown in fig. 6, with a restoring beam size similar to that of the X-ray color map shown in fig. 2. The resulting images were low-pass filtered to remove compact radio sources (supernova remnants and HII regions), using a box 7.6×7.6 arcsec. The smoothed images were combined to form a spectral index image (spectral index α , where $S_\nu \propto \nu^\alpha$), using regions with S/N of 10 or better in the smoothed images (fig. 7).

5. DISCUSSION

5.1. Properties of the Hot ISM

Fabbiano et al (2001) reported that the *Chandra* image of NGC4038/39 shows extended, soft emission features with dimensions ranging from a few arcseconds (few hundred parsecs) to the size of the entire galaxian system or larger. In §2 and §3 we have taken a closer look at this emission and at its spectral properties. Here we discuss the implications of these results for the properties of the hot ISM.

We used the results of the spectral analysis to estimate the physical parameters of the ISM in the two nuclear regions and in the most intense well-defined emission region in the N-W arm (R1, see fig 3b and Table 5), and to infer the supernova rate in these regions. We used the emission measures from the fit to the RS + (RS + PO) model (see Table 6). In this model we assume a cooler external unabsorbed ISM layer surrounding hotter ISM and harder sources of emission embedded in a cooler/dusty absorbing medium. This picture agrees with the true-color X-ray map, and suggests a hotter inner superbubble, heated by early-type stellar winds and supernovae, with an outflowing and cooling upper layer of ISM.

Our estimates are given in Table 7, for both low-kT (subscript 1), and high-kT (subscript 2) thermal components (from EM_1 and EM_2 of Table 6). For these calculations, we have assumed cylindrical emitting volumes of base given by the count extraction areas of Table 2. Although it is likely that hot absorbed emission originates from inner regions in a superbubble, with our data it is not possible to make an informed discrimination between the different geometries (even in projection on the sky) of the emitting regions. We assumed a height for the emitting cylinders of either 200 pc or 1 kpc. The thinner cylinder would correspond to an emission region of the approximate depth of a spiral disk, while the thicker cylinder assumes a scale-height more consistent with an outflowing hot ISM. We give both estimates in Table 7. We estimated thermal energy and cooling times following Tucker (1975) and using the intrinsic luminosities from Table 6. Thermal pressure in the assumption of electron and proton components in thermal equilibrium is $p = 2nkT$.

Supernova rates were derived as in Heckman et al (1996; see also Fabbiano et al 1997 for a similar approach applied to the ROSAT HRI image of the Antennae), which assumes that most of the mechanical energy supplied to the ambient medium in the star-forming regions is from supernovae. Following Heckman et al (1996), we adopt the relation for a superbubble: $E_{th} = 1.4 \times 10^{57} L_{mech,43} t_7$ ergs s^{-1} , where $L_{mech,43}$ is the mechanical energy supplied to the ambient medium in the star forming region from super-

novae, and t_7 is the age of the starburst in units of 10^7 yr. $L_{mech} = R_{SN} \times E_{SN}$, where R_{SN} is the supernova rate and $E_{SN} = 10^{51}$ ergs is the energy released in a supernova explosion. From this, we obtain an estimate of the supernova rate R_{SN} , equating E_{th} to our estimates of Table 7.

As shown by the X-ray/H α comparison in Paper I, in the nuclear regions the hot and warm ISM distributions closely follow each other, suggesting that the two gases are intermingled, as for example in the gaseous outflows of the nearby starburst nucleus M82 (Watson et al 1984). In this case the X-ray emitting volume may well be a fraction (η) of the one adopted here ($\eta = 1$ was assumed in Table 7). This would result in shorter cooling times ($\tau_c \sim \eta^{1/2}$) and similarly smaller thermal energies and supernova rates, while the thermal pressure would increase as $p \sim \eta^{-1/2}$.

The other region in Table 7 (R1) was identified in Paper I as a superbubble, with a hot core surrounded by H α filaments. As suggested in Paper I, R1 may be a more spectacular example of the superbubbles seen in more nearby galaxies such as the LMC and M101 (e.g. Wang & Helfand 1991; Williams & Chu 1995; see reviews in Chu 2000 and MacLow 2000).

We derive cooling times in the $10^7 - 10^8$ yr range and total masses of hot ISM in the $10^5 - 10^6 M_\odot$ for each region. For the two nuclear regions, where a comparison is possible, these hot gas masses are of order 1/1000 of the mass in cold molecular gas (Wilson et al 2000). The thermal pressures of the hot gas are of the order of a few $\times 10^{-11}$ dyn cm $^{-2}$. For the two nuclear regions, these pressures are remarkably similar to those that can be derived for the cold molecular clouds from the CO measurements of Zhu, Seaquist & Kuno (2003), suggesting a rough pressure equilibrium of the different phases of the ISM. Using the values of densities and temperatures from Zhu et al, we obtain cold gas pressures of 4.2×10^{-11} dyn cm $^{-2}$ and 3.1×10^{-11} dyn cm $^{-2}$ for the northern and southern nuclear regions, respectively. In both nuclei, for our assumption of gas volumes, the hotter X-ray components may have larger pressures, and create bubbles or even escape from the enveloping molecular clouds. However, we must remember that these estimates (both CO and X-rays) are only average values, depending on a number of assumptions, including the emitting volume and the small scale properties of the clouds (density and temperature structures) that cannot be measured at present.

In these regions our estimates of the supernova rates are within factors of a few of those estimated by Neff & Ulvestad (2000) from compact radio sources, on the basis of radio continuum observations at 6cm. We stress that the estimates in Table 7 are only indicative, given the uncertainties in the geometry of the emitting regions, and in the spectral models. If the 3-temperature RS+(RS+RS) model is used (see Table 5), the total emission measure would be larger for the northern nucleus. But even so, the estimates of the ISM parameters would not change much: this would result in a factor of < 2 increase in the mass of hot ISM, and correspondingly shorter cooling time. The estimates for the southern nucleus would not change appreciably; in this case the fit returns two low-temperature components with temperature and EM similar to those from the RS+(RS+PO) model, and a higher temperature

component, that may be related to harder emission from supernova remnants and X-ray binaries. In the case of R1, the results of this fit are probably unrealistic, requiring an extremely luminous, very low energy component.

5.2. Large-Scale Morphology of the Multi-Wavelength Diffuse Emission

Fig. 8 shows a comparison of the X-ray image of the diffuse emission (likely to be gas shock-heated by supernovae and stellar winds), with the HST WFPC-2 archival H α image (Whitmore et al 1999), that traces photoionization of the ISM by luminous O stars, and with the low-pass filtered 6cm radio continuum VLA image of fig. 6, to which both the low-energy spectrum of the warm and hot ISM, as well as non-thermal contributions from embedded supernova remnants, contribute. Fig. 9 compares the diffuse X-ray emission of fig. 2 (here plotted in red) with CO (Wilson et al 2000) and HI (Hibbard et al 2001) images.

These comparisons give a fairly complete picture of the large scale distribution of the different components of the ISM, and also of the effect of the extinction on the emission.

The regions where young stars are being formed in dusty molecular clouds, as traced by the CO, are also prominent in the radio continuum, that is not affected by cold-ISM/dust absorption. The radio continuum appears to follow the H α reasonably well, with the exception of the peak at the NE of the southern nucleus (the dusty star-forming ‘impact region’, Mirabel et al 1998; Wilson et al 2000; Zhang et al 2001). The radio spectral index map (fig. 7) indicates three regions where thermal emission ($\alpha > 0.0$) is present, probably from HII regions: the thickest part of the overlap region to the NE of NGC 4039 nucleus, another HII region complex further N and E of that, and a superbubble structure at the southern edge of the arc extending SW from the NGC 4038 nucleus. Filamentary structures in the non-thermal emission are evident running roughly EW across the northern half of the system, and may indicate magnetic field shears or discontinuities, given that the non-thermal emission in galaxies is from synchrotron. The X-ray emission has a distinct minimum in the ‘impact region’, which is likely to be due to absorption of the soft photons (the blue area in fig. 2). Mid-infrared ISO data have shown that this is the regions of most intense star formation, including stars as massive as $60 M_{\odot}$; the extinction in this region reaches $A_V = 70$ mag (Mirabel et al 1998). The blue area in fig. 2 can be seen trailing up to the northern nucleus (NGC 4038), following the region rich in dust lanes (see HST image in Whitmore et al 1999).

All wavebands trace well the spiral arm that appears to emerge on the SW side of the northern nucleus (NGC 4038), swings counter-clockwise and is easily traceable for about 90 deg in radio and X-ray. At that point, NW of the nucleus, the radio arm dims but continues its swing for another 90 degrees, as does the H α arm, and the HI emission. The diffuse X-ray emission instead is faint in this region. This region does not present any peculiarity in the mix of ages of stellar clusters (Zhang et al 2001), by comparison with other regions where diffuse X-ray emission is present, that would suggest a significantly older stellar population lacking the means of heating the ISM to X-ray temperatures. Hibbard et al

(2001) point out that the HI kinematics in this area suggest infall of HI onto NGC 4038. It may be possible that the infalling cold gas interact with and displace the hot gas. A general pattern of avoidance between cold and hot ISM can be seen for example in the merger remnant NGC 5128 (Karovska et al 2002). From the velocity maps and N_H in Hibbard et al (2001), we estimate an infall velocity for the HI cloud $v \sim 100$ km/s, and a mass density $\rho \sim 1.6 \times 10^{-24}$ g cm $^{-3}$, corresponding to 1 H atom per cubic centimeter. The ram pressure of this cloud would then be $\rho v^2 \sim 1.6 \times 10^{-10}$ dyn cm $^{-3}$, larger than the typical thermal pressure of the hot ISM (see Table 7). Our lowest estimate of the ram pressure is $\sim 3 \times 10^{-11}$ dyn cm $^{-3}$, comparable to the pressure estimates for the hot ISM. However, the pressures in Table 7 are derived for the most luminous X-ray regions, so are an overestimate of the pressure in the region of the northern spiral arm. We conclude that displacement of the hot ISM by infalling cold neutral hydrogen cloud is possible.

Interaction between cold and hot ISM is also suggested by the relative distribution of CO and X-ray emission. In the impact region, X-ray colors and spectra may suggest extinction as the cause of the low X-ray surface brightness, although, given the uncertainties in the fits, a situation with an embedded obscured hard component, and a ‘surface’ low-emission measure soft component, is also possible. However, the extinction interpretation would be in agreement with emission originating from a region of star formation deeply embedded in the molecular clouds, since the CO emission peaks in this area. Other CO/X-ray overlap or avoidance areas are not immediately ascribable to extinction. These regions include the X-ray gap in the NW spiral arm, and regions where the X-ray emission is instead intense: the ‘superbubble’ in the NW arm discussed in Paper I (regions R1 and R2 of fig. 3b), and the two nuclear regions. As we have shown in §5.1, the pressures in the cold (CO) and hot (X-ray) ISM are similar and suggest a situation where cold and hot ISM may be commingled and in equilibrium. Near the most intense region of diffuse X-ray emission at the southern nucleus (NGC 4039) there is a marked minimum of both HI and CO. This may suggest a hot nuclear outflow pushing aside the cold ISM, reminiscent of the morphology of M82 and NGC 253 (Watson et al 1984, Fabbiano & Trinchieri 1984).

6. SUMMARY AND CONCLUSIONS

This paper presents a first look at the complex hot ISM of the Antennae galaxies, based on the first *Chandra* observation of this merging system.

After producing an X-ray-color image, that gives us an immediate visual representation of the spectral complexity of the diffuse emission, we have obtained a quantitative estimate of this complexity by means of spectral fits. At least two temperatures (with different N_H) are needed to fit the most luminous regions, including the two nuclei, and what appear to be luminous superbubbles (Paper I) in the N-W star-forming arm of NGC 4038. The two temperatures are in the vicinities of 0.3 and 0.7 keV, with the hotter component being more highly absorbed. However, the fits (even adding a third component) are still not a good representation of the data. We have explored the effect of non-solar abundances in these fits. While the

fits improve for very low abundance values (as already reported with ASCA, Sansom et al 1996), they are still not good. Moreover, given the clear complexity of the emission field, suggested both by the X-ray-color image and by the spectral results, spuriously low value of the abundance may result because of a simplistic choice of fit models (e.g. Weaver et al 2000; Kim & Fabbiano 2003).

From these results we derive estimates of the hot ISM parameters for these three regions. We derive cooling times of $\sim 10^7 - 10^8$ yr and masses of hot ISM of $\sim 10^5 - 10^6 M_{\odot}$ for each region. In the two nuclei, these masses are much smaller than those present in molecular gas (Wilson et al 2000), but the thermal pressures of the two phases of the ISM are comparable, suggesting equilibrium. However, this conclusion depends on crucial assumption on the spatial distribution and filling factor of the ISM. It is also possible that, at least for the hottest component of the hot ISM, the thermal pressure may exceed that of the cold medium. For the two nuclear regions, where a comparison is possible, the supernova rates are of the order of magnitude of those estimated by Neff & Ulvestad (2000) for the same regions on the basis of radio continuum observations at 6cm.

We have compared the distribution of the diffuse X-ray emission with that of the 6cm radio continuum, H α (using an archival HST WFPC-2 image), HI (Hibbard et al 2001) and CO (Wilson et al 2000). While there is a general resemblance between different wavebands, that may

be related to a common link with star formation phenomena (Zhang et al 2001), this comparison shows significant differences. In particular, it shows very clearly the effect of obscuration on the X-ray emission, that has a minimum (where only hard photons escape) coincident with the large radio continuum and CO peaks in the impact region of the two galaxies. We also note a displacement of the diffuse X-ray emission on the northern side of the system, relative to the spiral arm visible in H α , radio continuum and HI. The HI velocities suggest infall in this region (Hibbard et al 2001), that results in a ram pressure exceeding the thermal pressure of the hot gas. This could explain the displacement of the X-ray emission towards the south.

These results demonstrate the richness of the ISM of the Antennae galaxies and justify further in dept-studies. A much deeper X-ray image is being collected with *Chandra* that will allow in time far more detailed studies of individual regions.

We thank the CXC DS and SDS teams for their efforts in reducing the data and developing the software used for the reduction (SDP) and analysis (CIAO). We thank our colleagues J. Hibbard and C. Wilson for providing the digital versions of their data that were used in this work, and D. Burke for help in producing fig. 6. The archival *Chandra* ACIS-S data used for this work was originally obtained as part of the GTO program (PI S. S. Murray). This work was supported by NASA contract NAS 8-39073 (CXC).

REFERENCES

Amram, P., Marcelin, M., Boulesteix, J., & le Coarer, E. 1992, A&A, 266, 106
 Anders, F. & Grevesse, N. 1989, Geochimica et Cosmochimica Acta, 53, 197
 Arnaud, K.A., 1996, Astronomical Data Analysis Software and Systems V, eds. Jacoby G. and Barnes J., ASP Conf. Series vol. 101
 Barnes, J. E. 1988, ApJ, 331, 699
 Bevington, P.R. & Robinson D.K., 1992, Data Reduction and Error Analysis for the Physical Sciences (McGraw Hill)
 Chu Y.-H. 2000, in 'Astrophysical Plasmas: Codels, Models and Observations', eds. J. Arthur, N. Brickhouse, J. Franco, RevMexAA (Serie de Conferencias), Vol 9, 262
 Fabbiano, G., Gioia, I. M., & Trinchieri, G. 1988, ApJ, 324, 749
 Fabbiano, G. & Trinchieri, G. 1983, ApJ, 266, L5
 Fabbiano, G. & Trinchieri, G. 1984, ApJ, 286, 491
 Fabbiano, G., Schweizer, F., & Mackie, G. 1997, ApJ, 478, 542
 Fabbiano, G. & Shapley, A. 2002, ApJ, 565, 908
 Fabbiano, G., Zezas, A., & Murray, S. 2001, ApJ, 554, 1035 (Paper I)
 Garmire, G. P. 1997, AAS, 190, 3404
 Heckman, T. M., Dahlem, M., Eales, S. A., Fabbiano, G., & Weaver, K. 1996, ApJ, 457, 616
 Hibbard, J. E., van der Hulst, J. M., Barnes, J. E., & Rich, R. M. 2001, AJ, 122, 2969
 Karovska, M., Fabbiano, G., Nicastro, F., Elvis, M., Kraft, R. P. & Murray, S. S. 2002, ApJ, in press (astro-ph/0205493)
 Kim, D.-W. & Fabbiano, G. 2003, ApJ, 586, 826
 Mac Low M.-M. 2000, in 'Astrophysical Plasmas: Codels, Models and Observations', eds. J. Arthur, N. Brickhouse, J. Franco, RevMexAA (Serie de Conferencias), Vol 9, 273
 Mengel, S., Lehnert, M. D., Thatte, N., Tacconi-Garman, L. E. and Genzel, R. 2000, ApJ, in press, Astro-ph/0010238
 Matsushita, K., Makishima, K., Rokutanda, E., Yamasaki, N. Y., & Ohashi, T. 1997, ApJ, 488, L125
 Mirabel, I. F., Vigroux, L., Charmandaris, V., Sauvage, M., Gallais, P., Tran, D., Cesarsky, C., Maddus, S. C., & Duc, P.-A. 1998, A&A, 333, L1
 Neff, S. G., & Ulvestad, J. S. 2000, AJ, 120, 670
 Read, A. M., Ponman, T. J., & Wolstencroft, R. D. 1995, MNRAS, 277, 397
 Raymond, J. C. & Smith, B. W. 1977, ApJS, 35, 419.
 Rubin, V. C., Ford, W. K., & D'Odorico, S. 1970, ApJ, 160, 801
 Sansom, A.E., Dotani, T., Okada, K., Yamashita, A., & Fabbiano, G. 1996, MNRAS, 281, 48
 Schulz N.S., 1999, ApJ, 511, 304
 Stanford, S. A., Sargent, A. I., Sanders, D. B., & Scoville, N. Z. 1990, ApJ, 349, 492
 Stark, A. A., Gammie, C. F., Wilson, R. W., Bally, J., Linke, R. A., Heiles, C., & Hurwitz, M. 1992, ApJS, 79, 77
 Toomre, A., & Toomre, J. 1972, ApJ, 178, 623
 Tucker, W. H. 1975 in 'Radiation processes in astrophysics', The MIT Press.
 Wang, Q., & Helfand, D. J. 1991, ApJ, 370, 541
 Watson, M. G., Stanger, V., & Griffiths, R. E. 1984, ApJ, 286, 144
 Weaver, K. A., Heckman, T. M., & Dahlem, M. 2000, ApJ, 534, 684
 Weisskopf, M., Tananbaum, H., Van Speybroeck, L. & O'Dell, S. 2000, Proc. SPIE 4012, p. 2 (astro-ph 0004127)
 Whitmore, B. C., & Schweizer, F. 1995, AJ, 109, 960
 Whitmore, B. C., Zhang, Q., Leitherer, C., Fall, S. M., Schweizer, F., Miller, B. W. 1999, ApJ, 118, 1551
 Williams R. M. & Chu, Y.-H. 1995, ApJ, 439, 132
 Wilson, C. D., Scoville, N., Madden, S. C., & Charmandaris, V. 2000, ApJ, 542, 120
 Yokogawa, J., Imanishi, K., Tsujimoto, M., Nishiuchi, M., Koyama, K., Nagase, F., & Corbet, R. H. D. 2000, ApJS, 128, 491
 Zezas, A., Fabbiano, G. Rots, A., & Murray, S., 2002, ApJS, in press (Paper II)
 Zezas, A., Fabbiano, G. Rots, A., & Murray, S., 2002, ApJ, in press (Paper III)
 Zezas, A. & Fabbiano, G. 2002, ApJ, in press (Paper IV)
 Zhang, Q., Fall, S. M., & Whitmore, B. C. 2001, ApJ, 561, 727
 Zhu, M., Seaquist, E. R., & Kuno, N. 2003, ApJ, 588, 243

FIG. 1.— Multi-color image of the Antennae prior to point source removal. Point sources to be removed are indicated by white ellipses. The color scale has been modified to enhance faint features.

FIG. 2.— Multi-color image after point source removal. The color scale has been modified to enhance faint features.

FIG. 3.— (a) Raw full band image of the Antennae after extracting the point sources indicated by their ellipses and numbered following the notation of Paper II. (b) Adaptively smoothed (0.3-6.0) keV band image of the diffuse emission of the Antennae, showing the regions used to extract the X-ray spectra.

FIG. 4.— Confidence contours for the RS+(RS) fits for the regions shown in Fig. 1b. Red contours correspond to the unabsorbed temperature component while blue contours correspond to the absorbed component. The crosses mark the best fit parameters.

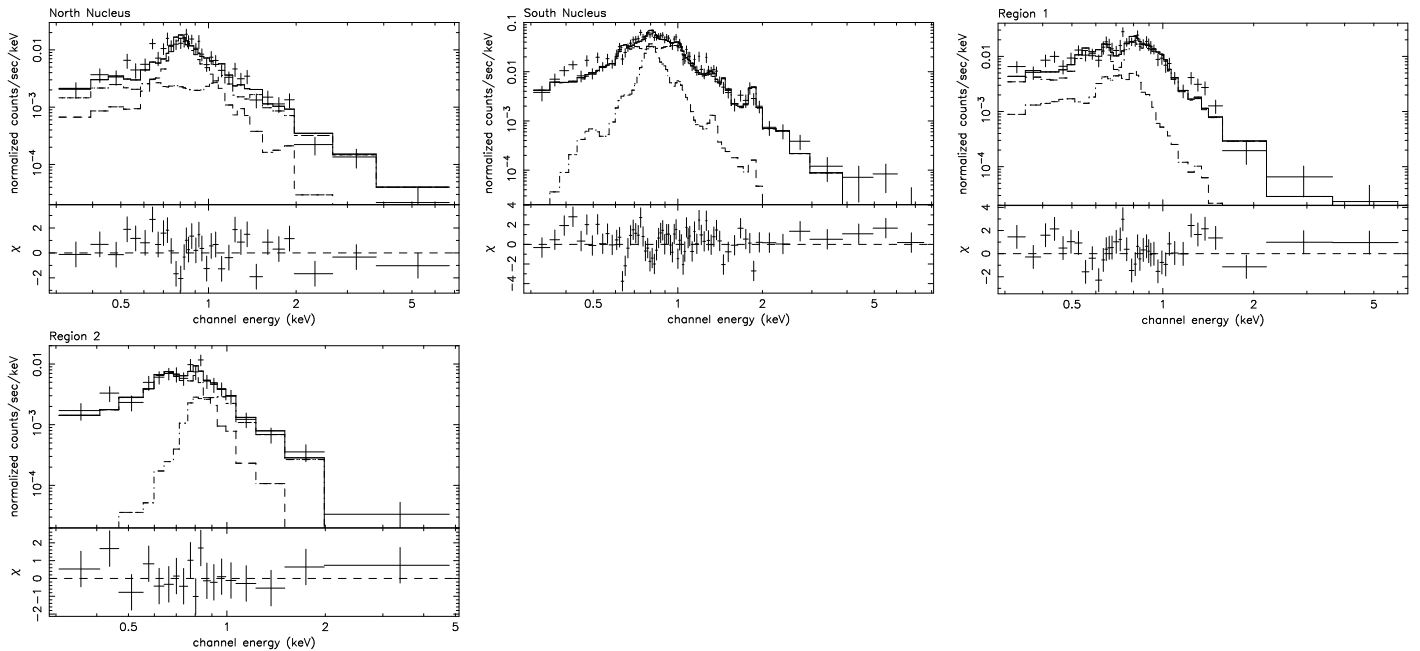


FIG. 5.— Spectra of the Northern and Southern nucleus and Regions 1 and 2 (see text for details) together with the best fit solar abundance RS+(RS) model and the residuals in σ . The dashed and dot-dashed lines show the two thermal components.

FIG. 6.— Image of the low-filtered diffuse radio emission in NGC4038/4039 at 6cm(left) and at 20cm(right). Both images have been restored with a beam $6.59'' \times 4.25''$, and smoothed with a $7.6'' \times 7.6''$ low-pass filter to remove the compact radio sources. The 20cm image has an rms of 52mJy/beam, the 6cm image has an rms of 18mJy/beam.

FIG. 7.— Gray-scale representation of the diffuse emission's 20-6cm spectral index distribution in NGC4038/9. This image shows only regions where both input images have a flux density of at least 10σ . The majority of the diffuse emission has a spectral index $\alpha < -0.5$ ($S_\nu \propto \nu^\alpha$) implying non-thermal synchrotron emission from relativistic electrons. Three regions have $\alpha > -0.5$; all are locations of significant current star-formation. Filamentary structures in the non-thermal emission probably indicates shocks and/or regions of magnetic field compression.

FIG. 8.— Radio/X-ray image of the diffuse emission in the Antennae. The radio image (green) is from the 6 cm low-pass filtered image in fig. 6. The X-ray image (red) is from the (0.3-6.0) keV band and is adaptively smoothed. The countours give sketchy outlines of the $H\alpha$ emission from the HST WFPC2 data (see Paper I), and identify the most active HII regions. The circles in the bottom right of the image indicate the resolution of the radio and X-ray bands. In the case of the X-ray band they indicate the minimum and the maximum smoothing scales.

FIG. 9.— A combined HI (red), CO (green), and X-ray (blue) image of the Antennae. The HI data are from the maps of Hibbard et al. (2001) and the CO data are from Wilson et al. (2001). The X-ray data are in the (0.3-6.0) keV band. The circles in the bottom right of the figure indicate the resolution of each image. For the X-ray band they indicate the minimum and the maximum smoothing scales.

TABLE 1
SPECTRAL FITS FOR THE TEMPERATURE MAP ($Z = Z_{\odot}$)

Region (1)	Net counts (2)	$N_{\text{H, tot}}^{\text{a}}$ (3)	kT_1^{b} (4)	N_{H}^{c} (5)	kT_2^{d} (6)	EM_1/EM_2 (7)	χ^2 (dof) (8)
1-A ^e	33.4 ± 13.1	$0.22_{-0.19}^{+0.44}$	$0.1(< 0.2)$				5.4 (8)
1-B ^e	135.1 ± 16.7	$0.60_{-0.27}^{+0.17}$	$0.14_{-0.07}^{+0.06}$				13.3 (14)
1-C	285.4 ± 20.6	$0.034(< 0.1)$	$0.28_{-0.04}^{+0.03}$	< 0.17	$5.74_{-5.67}^{+0.26}$	0.52	22.6 (19)
1-D	247.4 ± 19.4	$0.034(< 0.09)$	$0.20_{-0.04}^{+0.04}$	$0.30_{-0.30}^{+0.28}$	$0.70_{-0.13}^{+0.10}$	0.79	9.5 (17)
1-E ^e	130.2 ± 16.6	$0.71_{-0.19}^{+0.86}$	$0.14_{-0.08}^{+0.03}$				15.0 (14)
2-A	207.9 ± 18.5	$0.94_{-0.26}^{+0.33}$	$0.09_{-0.02}^{+0.03}$	> 3.19	$6.6(> 0.7)$	12300	11.1 (15)
2-B	767.0 ± 30.1	$0.034(< 0.063)$	$0.26_{-0.04}^{+0.03}$	$0.38_{-0.15}^{+0.15}$	$0.69_{-0.07}^{+0.06}$	0.37	44.3 (38)
2-C	1520.7 ± 40.7	$0.018_{-0.016}^{+0.027}$	$0.31_{-0.02}^{+0.20}$	$0.67_{-0.11}^{+0.13}$	$0.71_{-0.03}^{+0.50}$	0.25	123.0 (58)
2-D	554.4 ± 26.4	$0.034(< 0.087)$	$0.26_{-0.03}^{+0.02}$	$0.38_{-0.35}^{+0.28}$	$0.85_{-0.13}^{+0.13}$	0.60	44.1 (31)
2-E	549.7 ± 26.4	$0.034(< 0.056)$	$0.26_{-0.03}^{+0.04}$	$0.37_{-0.37}^{+0.22}$	$0.72_{-0.07}^{+0.28}$	0.89	48.7 (29)
3-A	928.2 ± 32.5	$0.034(< 0.054)$	$0.25_{-0.03}^{+0.05}$	$0.41_{-0.17}^{+0.12}$	$0.70_{-0.06}^{+0.07}$	0.39	44.7 (46)
3-B	866.5 ± 31.4	$0.04_{-0.01}^{+0.05}$	$0.25_{-0.03}^{+0.03}$	$0.70_{-0.14}^{+0.12}$	$0.72_{-0.04}^{+0.06}$	0.15	54.7 (42)
3-C	751.0 ± 29.9	$0.79_{-0.19}^{+0.26}$	$0.11_{-0.02}^{+0.03}$	> 0.12	$0.61_{-0.19}^{+0.08}$	209	39.9 (41)
3-D	694.6 ± 28.6	$0.034(< 0.049)$	$0.25_{-0.03}^{+0.03}$	$0.44_{-0.18}^{+0.15}$	$0.69_{-0.06}^{+0.08}$	0.35	40.6 (36)
3-E	794.7 ± 30.5	$0.034(< 0.052)$	$0.21_{-0.02}^{+0.03}$	$0.24_{-0.24}^{+0.15}$	$0.69_{-0.06}^{+0.12}$	0.77	58.9 (42)
4-A ^e	202.0 ± 18.3	$0.81_{-0.22}^{+0.11}$	$0.15_{-0.22}^{+0.14}$				15.1 (17)
4-B	368.0 ± 22.1	$0.034(< 0.11)$	$0.30_{-0.06}^{+0.05}$	$0.80_{-0.35}^{+0.20}$	$0.88_{-0.12}^{+0.12}$	0.09	23.2 (23)
4-C	483.1 ± 24.9	$0.06_{-0.02}^{+0.08}$	$0.26_{-0.04}^{+0.04}$	$0.26_{-0.26}^{+0.28}$	$0.79_{-0.10}^{+0.09}$	0.58	16.6 (26)
4-D	264.6 ± 20.3	$0.034(< 0.94)$	$0.26_{-0.04}^{+0.05}$	$0.41_{-0.41}^{+0.42}$	$0.78_{-0.16}^{+0.22}$	0.60	12.6 (18)
4-E	127.2 ± 16.5	$0.034(< 0.1)$	$0.28_{-0.03}^{+0.03}$	$0.99_{-1.00}^{+47.0}$	> 2.24	0.33	11.3 (11)
5-A	141.7 ± 17.0	$1.4_{-0.54}^{+1.1}$	$0.07_{-0.03}^{+0.05}$	$8.45_{-8.45}^{+4.45}$	$0.35_{-0.27}^{+20.6}$	654.4	8.3 (11)
5-B	714.4 ± 29.1	$0.034(< 0.079)$	$0.30_{-0.06}^{+0.03}$	$0.37_{-0.18}^{+0.13}$	$0.83_{-0.09}^{+0.09}$	0.28	46.5 (38)
5-C	2101.0 ± 47.3	$0.034(< 0.047)$	$0.30_{-0.02}^{+0.02}$	$0.42_{-0.10}^{+0.10}$	$0.78_{-0.05}^{+0.05}$	0.32	104.5 (68)
5-D	374.2 ± 22.7	$0.034(< 0.06)$	$0.30_{-0.12}^{+0.05}$	< 0.29	$0.71_{-0.13}^{+0.16}$	1.76	28.0 (22)
5-E	131.9 ± 16.5	$0.39_{-0.36}^{+0.36}$	$0.28_{-0.10}^{+0.12}$	> 17.9	$0.22_{-0.07}^{+0.01}$	<0.0001	11.2 (11)
6-A ^e	116.2 ± 16.1	$0.034(< 0.126)$	$0.27_{-0.05}^{+0.03}$				11.7 (13)
6-B ^e	150.6 ± 17.1	$0.89_{-0.18}^{+0.22}$	$0.12_{-0.03}^{+0.03}$				14.1 (15)
6-C	293.9 ± 20.7	$0.23_{-0.20}^{+0.23}$	$0.13_{-0.06}^{+0.06}$	< 0.29	$0.48_{-0.17}^{+0.15}$	3.90	15.5 (18)
6-D	139.7 ± 16.8	$0.034(< 0.15)$	$0.33_{-0.07}^{+0.11}$	< 0.52	$1.26_{-0.26}^{+0.77}$	0.52	8.2 (11)

^{a,c} Absorbing column density for total spectrum (a) and the second thermal component (c) in units of 10^{22} cm^{-2} . Quoted errors are at the 90% confidence level for one interesting parameter.

^{b,d} Temperature for the unabsorbed (b) and the absorbed (d) thermal component in keV. Quoted errors are at the 90% confidence level for one interesting parameter.

^e Fits with only one thermal component.

TABLE 2
SPECTRAL FITS FOR THE TEMPERATURE MAP (FREE ABUNDANCE)

Region (1)	$N_{H,\text{tot}}^a$ (2)	kT_1^b (3)	Z^e (4)	N_{H}^c (5)	kT_2^d (6)	Z^f (7)	EM_1/EM_2 (8)	χ^2 (dof) (9)
1-A ^g	$0.58^{+1.01}_{-0.54}$	$0.05^{+0.18}_{-0.03}$	$0.02(<5.0)$					3.3/7
1-B ^g	$0.24(<0.678)$	$0.22^{+0.10}_{-0.02}$	$0.03^{+0.26}_{-0.021}$					9.7/13
1-C	$0.15^{+0.21}_{-0.12}$	$0.28^{+0.05}_{-0.08}$	$0.04^{+4.96}_{-0.03}$	<9.02	64.0^h	5.00^h	19.02	20.0/17
1-D	$0.03^{+0.08}_{-0.00}$	$0.21^{+0.05}_{-0.05}$	$0.24^{+4.76}_{-0.19}$	$0.36^{+0.30}_{-0.36}$	$0.70^{+0.15}_{-0.13}$	$4.00(>0.26)$	6.96	9.1/15
1-E ^g	$0.19(<1.05)$	$0.03(<0.24)$	$0.28^{+0.23}_{-0.19}$					11.2/12
2-A	$0.74^{+0.39}_{-0.45}$	$0.11^{+0.13}_{-0.04}$	$0.03^{+0.42}_{-0.03}$	$0.85^{+4.76}_{-0.85}$	$4.48(>0.45)$	5.00^h	9012	7.8/13
2-B	$0.03^{+0.06}_{-0.00}$	$0.27^{+0.06}_{-0.05}$	$0.27^{+4.73}_{-0.18}$	$0.30^{+0.28}_{-0.26}$	$0.70^{+0.07}_{-0.07}$	$0.45(>0.14)$	0.70	42.5/36
2-C	$0.03^{+0.05}_{-0.00}$	$0.31^{+0.03}_{-0.03}$	$0.33^{+4.67}_{-0.22}$	$0.25^{+0.31}_{-0.14}$	$0.71^{+0.07}_{-0.03}$	$0.09^{+0.24}_{-0.04}$	0.24	111.5/56
2-D	$0.06^{+0.06}_{-0.02}$	$0.27^{+0.03}_{-0.05}$	$4.90^{+0.10}_{-4.52}$	$0.02^{+0.36}_{-0.02}$	$0.89^{+0.10}_{-0.12}$	$0.14^{+0.20}_{-0.09}$	0.05	38.9/29
2-E	$0.03^{+0.05}_{-0.00}$	$0.30^{+0.04}_{-0.03}$	$0.21^{+0.41}_{-0.13}$	$1.90^{+1.02}_{-0.90}$	$0.09^{+0.04}_{-0.01}$	$4.55^{+0.45}_{-4.45}$	0.0001	37.3/27
3-A	$0.06^{+0.06}_{-0.02}$	$0.27^{+0.06}_{-0.04}$	$0.13^{+0.25}_{-0.07}$	$0.40^{+0.22}_{-0.34}$	$0.69^{+0.10}_{-0.06}$	$1.29^{+3.71}_{-1.10}$	3.54	38.3/44
3-B	$0.13^{+0.15}_{-0.09}$	$0.25^{+0.06}_{-0.06}$	$0.07^{+0.41}_{-0.05}$	$0.64^{+0.16}_{-0.27}$	$0.72^{+0.07}_{-0.05}$	$1.12^{+3.88}_{-0.86}$	3.00	51.1/40
3-C	$0.29^{+0.30}_{-0.16}$	$0.22^{+0.07}_{-0.07}$	$0.02^{+4.98}_{-0.02}$	<0.36	$0.77^{+0.11}_{-0.10}$	$0.16^{+1.38}_{-0.10}$	14.68	25.8/39
3-D	$0.03^{+0.04}_{-0.00}$	$0.30^{+0.06}_{-0.06}$	$0.11^{+0.10}_{-0.05}$	$0.53^{+0.19}_{-0.32}$	$0.70^{+0.09}_{-0.06}$	$4.99(>0.39)$	10.52	28.8/34
3-E	$0.03^{+0.06}_{-0.00}$	$0.23^{+0.04}_{-0.05}$	$1.38^{+3.62}_{-1.28}$	<0.35	$0.71^{+0.09}_{-0.08}$	$0.13^{+1.49}_{-0.05}$	0.11	45.1/40
4-A ^g	$0.37^{+1.13}_{-0.19}$	$0.27^{+0.11}_{-0.20}$	$0.05^{+0.11}_{-0.04}$					11.6/16
4-B	$0.06^{+0.20}_{-0.03}$	$0.35^{+0.24}_{-0.09}$	$0.09^{+0.69}_{-0.07}$	$0.67^{+0.37}_{-0.55}$	$0.91^{+0.21}_{-0.14}$	$0.45^{+4.55}_{-0.36}$	0.52	19.7/21
4-C	$0.16^{+0.17}_{-0.13}$	$0.26^{+0.08}_{-0.07}$	$0.07^{+4.93}_{-0.05}$	$0.20^{+0.37}_{-0.20}$	$0.79^{+0.14}_{-0.11}$	$1.42^{+3.58}_{-1.31}$	16.47	14.0/24
4-D	$0.03^{+0.10}_{-0.00}$	$0.29^{+0.07}_{-0.07}$	$0.20^{+4.80}_{-0.15}$	$0.52^{+0.52}_{-0.52}$	$0.79^{+0.24}_{-0.15}$	$4.99^{+0.01}_{-4.74}$	10.34	11.1/16
4-E	$0.03^{+0.16}_{-0.00}$	$0.30^{+0.10}_{-0.05}$	$0.13^{+4.87}_{-0.10}$	$5.93^{+44.6}_{-5.93}$	$1.44(>0.64)$	5.00^h	1.09	10.0/9
5-A	$1.12^{+1.11}_{-1.02}$	$0.08^{+0.32}_{-0.04}$	$0.03^{+4.97}_{-0.03}$	$10.9^{+33.8}_{-10.9}$	$0.27^{+2.57}_{-0.20}$	$0.03^{+4.97}_{-0.03}$	5.10	6.2/9
5-B	$0.09^{+0.14}_{-0.06}$	$0.32^{+0.08}_{-0.07}$	$0.13^{+1.18}_{-0.09}$	$0.40^{+0.21}_{-0.40}$	$0.83^{+0.14}_{-0.09}$	$3.36^{+1.64}_{-3.07}$	7.21	44.1/36
5-C	$0.03^{+0.06}_{-0.00}$	$0.34^{+0.04}_{-0.04}$	$0.41^{+4.59}_{-0.30}$	$0.13^{+0.14}_{-0.13}$	$0.82^{+0.06}_{-0.06}$	$0.18^{+0.19}_{-0.06}$	0.25	84.8/66
5-D	$0.05^{+0.08}_{-0.01}$	$0.42^{+0.10}_{-0.06}$	$0.13^{+0.11}_{-0.05}$	$89.1^{+42.9}_{-83.6}$	$0.17^{+0.04}_{-0.04}$	4.83^h	<0.0001	21.9/20
5-E	$0.39^{+0.33}_{-0.33}$	$0.28^{+0.14}_{-0.10}$	$0.16^{+4.85}_{-0.12}$	$118.2^{+27.0}_{-45.7}$	$0.17^{+0.08}_{-0.03}$	4.32^h	<0.0001	10.5/9
6-A ^g	$0.034(<0.16)$	$0.31^{+0.10}_{-0.07}$	$0.06^{+0.18}_{-0.04}$					6.4/12
6-B ^g	$0.79^{+0.38}_{-0.44}$	$0.12^{+0.10}_{-0.03}$	0.04^h					6.4/12
6-C	$0.14^{+0.11}_{-0.09}$	$0.41^{+0.12}_{-0.08}$	$0.10^{+0.09}_{-0.04}$	$10.8^{+9.20}_{-10.8}$	63.9^h	0.88^h	5.30	18.1/16
6-D	$0.03(0.36)$	$0.36^{+0.27}_{-0.13}$	0.12^h	<1.18	$0.31^{+5.98}_{-0.75}$	5.00^h	15.79	7.2/9

^{a,c} Absorbing column density for total spectrum (a) and the second thermal component (c) in units of 10^{22} cm $^{-2}$. Quoted errors are at the 90% confidence level for one interesting parameter.

^{b,d} Temperature for the unabsorbed (b) and the absorbed (d) thermal component in keV. Quoted errors are at the 90% confidence level for one interesting parameter.

^{e,f} Abundance for the unabsorbed (b) and the absorbed (d) thermal component in keV. Quoted errors are at the 90% confidence level for one interesting parameter.

^g Fits with only one thermal component.

^h Unconstrained parameter (1 σ range greater than allowed range for the parameter).

TABLE 3
SPECTRAL FITS FOR SELECTED REGIONS (Z=Z \odot)

Region Net counts \pm error	RA (J2000) Dec (J2000) Area (sq. arcsec)	RS+(PO) $N_{H,\text{tot}}^a$ N_H^c	RS+(RS) $N_{H,\text{tot}}^a$ N_H^c	kT_1^b Γ χ^2 (dof)	kT_1^b kT_2^d χ^2 (dof)
(1)	(2)	(3)	(5)	(4)	(6)
North Nucleus 604.7 ± 25.4	12: 01: 52.8 -18: 52: 08.5 222	0.034(< 0.2) 0.15(< 0.28)	0.034(< 0.045)	$0.65_{-0.08}^{+0.06}$ $2.9_{-0.5}^{+0.7}$ 38.9 (29)	$0.65_{-0.06}^{+0.03}$ $3.04_{-0.79}^{+1.4}$ 52.3 (29)
South Nucleus 2180.4 ± 47.5	12: 01: 53.9 -18: 53: 08.5 488	0.034(< 0.058) 0.22 $_{-0.09}^{+0.03}$	0.034(< 0.045)	$0.76_{-0.03}^{+0.03}$ $3.4_{-0.5}^{+0.7}$ 138.7 (67)	$0.32_{-0.03}^{+0.02}$ $0.79_{-0.04}^{+0.05}$ 125.1 (67)
Region 1 780.3 ± 28.9	12: 01: 50.4 -18: 52: 19.1 235	0.034(< 0.08) 0.12 $_{-0.09}^{+0.09}$	0.034(< 0.05)	$0.65_{-0.05}^{+0.05}$ $3.98_{-0.64}^{+0.73}$ 64.9 (34)	$0.20_{-0.02}^{+0.05}$ $0.78_{-0.06}^{+0.06}$ 58.9 (34)
Region 2 302.0 ± 18.0	12: 01: 50.6 -18: 52: 04.3 137	0.11(< 0.27) < 0.45	0.034(< 0.08)	$0.33_{-0.06}^{+0.09}$ $2.8_{-0.8}^{+1.3}$ 14.9 (13)	$0.27_{-0.04}^{+0.04}$ $0.51_{-0.36}^{+0.44}$ 11.2 (13)

^{a,c} Absorbing column density for the total spectrum in units of 10^{22} cm $^{-2}$. Quoted errors are at the 90% confidence level for one interesting parameter.

^{b,d} Temperature of the thermal component in units of keV. Quoted errors are at the 90% confidence level for one interesting parameter.

TABLE 4
SPECTRAL FITS FOR SELECTED REGIONS (FREE ABUNDANCE)

Region	RS+(PO)			RS+(RS)		
	$N_{H,\text{tot}}^a$	kT_1^b	χ^2 (dof)	$N_{H,\text{tot}}^a$	kT_1^b	Z_1^e
(1)	N_H^c	Γ	(2)	N_H^c	kT_2^d	Z_2^d
North Nucleus	0.14(< 0.23)	$0.63_{-0.25}^{+0.07}$	0.06(< 0.15)	$0.3_{-0.06}^{+0.08}$	$0.17_{-0.07}^{+1.89}$	
	3.4(< 30.3)	$3.12_{-3.18}^{+6.8}$	$0.46_{-0.31}^{+0.45}$	$0.7_{-0.1}^{+0.12}$	$0.12_{-0.19}^{+0.19}$	
	$0.10_{-0.02}^{+0.02}$	37.5 (28)	$0.46_{-0.31}^{+0.45}$	32.5 (27)		
South Nucleus	$0.10_{-0.02}^{+0.02}$	$0.74_{-0.07}^{+0.03}$	0.034(< 0.1)	$0.35_{-0.02}^{+0.06}$	0.22(> 0.08)	
	2.5(< 180.3)	-0.45(< 6.5)	$0.17_{-0.16}^{+0.13}$	$0.82_{-0.05}^{+0.05}$	$0.23_{-0.13}^{+0.27}$	
	$0.14_{-0.05}^{+0.05}$	135.1 (66)		99.3 (65)		
Region 1	0.034(< 0.108)	$0.37_{-0.07}^{+0.14}$	0.034(< 0.105)	$0.26_{-0.07}^{+0.09}$	0.09(> 0.02)	
	$1.24_{-0.49}^{+0.33}$	9.34(> 6.37)	0.05(< 0.36)	$0.73_{-0.09}^{+0.09}$	0.29(> 0.09)	
	$0.07_{-0.03}^{+0.08}$	41.8 (33)		41.7 (32)		

^{a,c} Absorbing column density for the total spectrum in units of 10^{22} cm^{-2} . Quoted errors are at the 90% confidence level for one interesting parameter.

^{b,d} Temperature of the thermal component in units of keV. Quoted errors are at the 90% confidence level for one interesting parameter.

TABLE 5
SPECTRAL FITS FOR SELECTED REGIONS (Z=Z \odot)

Region	RS ₁ + (RS ₂ +PO)			RS ₁ + RS ₂ + (PO)			RS ₁ + (RS ₂ +RS ₃)			RS ₁ + RS ₂ + (RS ₃)		
	$N_{H,\text{tot}}^a$	kT_1^b	χ^2 (dof)	$N_{H,\text{tot}}^a$	kT_1^b	χ^2 (dof)	$N_{H,\text{tot}}^a$	kT_1^b	χ^2 (dof)	$N_{H,\text{tot}}^a$	kT_1^b	χ^2 (dof)
(1)	N_H^c	kT_2^d	Γ	N_H^c	kT_2^d	Γ	kT_3^d	χ^2 (dof)	(7)	N_H^c	kT_2^b	χ^2 (dof)
North Nucleus	0.034(< 0.18)	$0.28_{-0.06}^{+0.09}$	0.034(< 0.21)	$0.28_{-0.09}^{+0.10}$	0.034(< 0.72)	$0.28_{-0.04}^{+0.03}$	0.034(< 0.075)	$0.29_{-0.05}^{+0.05}$				
	0.24(< 0.69)	$0.70_{-0.11}^{+0.11}$	0.27(< 0.83)	$0.72_{-0.11}^{+0.13}$	$0.73_{-0.40}^{+0.19}$	$0.65_{-0.07}^{+0.10}$	$0.68_{-0.37}^{+0.20}$	8.1(> 2.7)				
	$2.87_{-0.64}^{+1.08}$	30.0 (27)	$2.96_{-0.59}^{+1.44}$	30.6 (27)	16.2(> 1.9)	33.2 (27)	$0.66_{-0.09}^{+0.09}$	30.7 (27)				
South Nucleus	0.034(< 0.10)	$0.35_{-0.03}^{+0.06}$	0.034(< 0.15)	$0.37_{-0.03}^{+0.06}$	0.034(< 0.072)	$0.36_{-0.04}^{+0.05}$	0.053(< 0.073)	$0.36_{-0.03}^{+0.05}$				
	$0.15_{-0.12}^{+0.11}$	$0.82_{-0.04}^{+0.06}$	0.33(< 0.6)	$0.85_{-0.05}^{+0.06}$	0.03(< 0.08)	$0.85_{-0.04}^{+0.05}$	< 0.09	$0.85_{-0.03}^{+0.11}$				
	$2.9_{-0.5}^{+0.8}$	99.7 (65)	$3.47_{-1.09}^{+1.24}$	101.2 (65)	$2.9_{-0.08}^{+2.0}$	112.8 (65)	$2.94_{-0.82}^{+1.92}$	113.1 (65)				
Region 1	0.034(< 0.13)	$0.25_{-0.06}^{+0.07}$	0.06(< 0.14)	$0.25_{-0.09}^{+0.08}$	$0.21_{-0.13}^{+0.12}$	$0.07_{-0.03}^{+0.03}$	$0.23_{-0.10}^{+0.10}$	$0.06_{-0.02}^{+0.05}$				
	0.05(< 0.19)	$0.74_{-0.09}^{+0.08}$	< 0.32	$0.75_{-0.08}^{+0.08}$	0.05(< 0.3)	$0.28_{-0.05}^{+0.04}$	0.032(< 0.29)	$0.28_{-0.05}^{+0.04}$				
	$3.53_{-0.9}^{+4.0}$	42.4 (32)	$3.37_{-0.87}^{+1.58}$	42.6 (32)	$0.79_{-0.08}^{+0.11}$	42.8 (32)	$0.79_{-0.11}^{+0.10}$	42.9 (32)				

^{a,c} Absorbing column density for the total spectrum (a) and the hard component (c) in units of 10^{22} cm^{-2} . Quoted errors are at the 90% confidence level for one interesting parameter.

^{b,d} Temperature of the unabsorbed (b) and absorbed (d) thermal component in units of keV. Quoted errors are at the 90% confidence level for one interesting parameter.

TABLE 6
INTENSITY OF SPECTRAL COMPONENTS (Z=Z_⊕)

Region	RS ₁ + (RS ₂ +PO)		RS ₁ + RS ₂ +(PO)		RS ₁ + (RS ₂ +RS ₃)		RS ₁ + RS ₂ + (RS ₃)	
(1)	EM ₁ ^a (L _X)	EM ₂ ^b (L _X)	EM ₁ ^a (L _X)	EM ₂ ^b (L _X)	EM ₁ ^a (L _X)	EM ₂ ^b (L _X)	EM ₁ ^a (L _X)	EM ₂ ^b (L _X)
	Norm. ^c (L _X)	(2)	Norm. ^c (L _X)	(4)	EM ₃ ^d (L _X)	(6)	EM ₃ ^d (L _X)	(8)
North Nucleus	2.9 (0.38)	5.3 (0.89)	2.3 (0.30)	2.6 (0.43)	4.62 (0.60)	28.8 (4.96)	4.03 (0.52)	4.87 (0.47)
	7.9 (4.53)		9.6 (6.28)		4.21 (0.40)		22.8 (3.93)	
South Nucleus	9.7 (1.32)	26.1 (3.70)	8.9 (1.24)	17.1 (2.34)	10.1 (1.39)	21.2 (2.88)	10.9 (1.52)	20.3 (2.74)
	11.9 (7.38)		23.7 (33.0)		16.5 (1.27)		16.6 (1.28)	
Region 1	4.6 (0.60)	5.8 (0.92)	5.6 (0.73)	5.4 (0.86)	350.2 (338.7)	17.4 (2.25)	95.6 (96.6)	19.7 (2.54)
	2.6 (3.95)		2.4 (3.04)		8.4 (1.26)		7.95 (1.19)	
Region 2 ^e	3.4 (0.44)	6.2 (0.90)			4.0 (0.53)			
					2.4 (1.27)			

^{a,b} Emission Measure for the low (a) and high (b) temperature component in units of $10^8 \times (4\pi D^2)$ cm⁻³ where D is the distance. In parentheses, absorption-corrected luminosity in the 0.1-10.0keV band, in units of 10^{39} erg s⁻¹

^c Normalization of the PO component (at 1 keV) in units of 10^{-6} photons/keV/cm²/s. In parentheses, absorption-corrected luminosity in the 0.1-10.0keV band, in units of 10^{39} erg s⁻¹

^d Emission Measure (and luminosity) for the third thermal component. The units are the same as in the first two components.

^e The parameters for Region 2 correspond to the RS+(PO) and RS+(RS) models instead of the RS+(RS+PO) and RS+(RS+RS) models respectively.

TABLE 7
ESTIMATED ISM PARAMETERS

Region	n (10^{-2} cm ⁻³)	E_{th} (10^{54} ergs)	τ_c (10^7 yrs)	M_{ISM} ($10^6 M_{\odot}$)	p 10^{-11} dyn cm ⁻²	SNR (10^{-3} yrs ⁻¹)
North Nucleus	3.3 ₁ , 4.5 ₂ (1.5 ₁ , 2.0 ₂) ^a	0.5 ₁ , 1.6 ₂ (1.2 ₁ , 3.6 ₂)	5 ₁ , 6 ₂ (10 ₁ , 13 ₂)	0.3 ₁ , 0.4 ₂ (0.7 ₁ , 0.9 ₂)	3.1 ₁ , 10.7 ₂ (1.4 ₁ , 4.8 ₂)	0.2 (0.3)
South Nucleus	1.9 ₁ , 3.2 ₂ (0.9 ₁ , 1.4 ₂)	3.0 ₁ , 14 ₂ (7.1 ₁ , 30 ₂)	7.7 ₁ , 12 ₂ (18 ₁ , 27 ₂)	1.7 ₁ , 3 ₂ (4 ₁ , 6.4 ₂)	2.3 ₁ , 8.9 ₂ (1.1 ₁ , 3.9 ₂)	1.2 (3.0)
Region 1	2.2 ₁ , 2.5 ₂ (1.0 ₁ , 1.1 ₂)	1.0 ₁ , 3.5 ₂ (2.1 ₁ , 7.7 ₂)	5.4 ₁ , 13 ₂ (12 ₁ , 28 ₂)	0.7 ₁ , 0.8 ₂ (1.6 ₁ , 1.7 ₂)	1.9 ₁ , 6.3 ₂ (0.8 ₁ , 2.8 ₂)	0.3 (0.7)

¹Lower temperature RS component

²Higher temperature RS component

^aFor an emitting cylinder of height 200 pc; values in parentheses are for a 1000 pc height cylinder

This figure "f1.jpg" is available in "jpg" format from:

<http://arxiv.org/ps/astro-ph/0308145v1>

This figure "f2.jpg" is available in "jpg" format from:

<http://arxiv.org/ps/astro-ph/0308145v1>

This figure "f3a.jpg" is available in "jpg" format from:

<http://arxiv.org/ps/astro-ph/0308145v1>

This figure "f3b.jpg" is available in "jpg" format from:

<http://arxiv.org/ps/astro-ph/0308145v1>

This figure "f4.jpg" is available in "jpg" format from:

<http://arxiv.org/ps/astro-ph/0308145v1>

This figure "f6.jpg" is available in "jpg" format from:

<http://arxiv.org/ps/astro-ph/0308145v1>

This figure "f7.jpg" is available in "jpg" format from:

<http://arxiv.org/ps/astro-ph/0308145v1>

This figure "f8.jpg" is available in "jpg" format from:

<http://arxiv.org/ps/astro-ph/0308145v1>

This figure "f9.jpg" is available in "jpg" format from:

<http://arxiv.org/ps/astro-ph/0308145v1>